Monthly Notices of the Royal Astronomical Society

Mon. Not. R. Astron. Soc. **410,** 2025–2042 (2011) doi:10.1111/j.1365-2966.2010.17579.x

The earliest galaxies seen in 21 cm line absorption

Yidong Xu,[1,2,3]★ Andrea Ferrara[4] and Xuelei Chen[3,5]

[1]*Department of Astronomy, School of Physics, Peking University, Beijing 100871, China*
[2]*SISSA/International School for Advanced Studies, Via Beirut 4, 34014 Trieste, Italy*
[3]*National Astronomical Observatories, Chinese Academy of Sciences, Beijing 100012, China*
[4]*Scuola Normale Superiore, Piazza dei Cavalieri 7, 56126 Pisa, Italy*
[5]*Center for High Energy Physics, Peking University, Beijing 100871, China*

Accepted 2010 August 22. Received 2010 August 20; in original form 2009 October 22

ABSTRACT

We investigate the 21 cm absorption lines produced by non-linear structures during the early stage of reionization, i.e. the starless minihaloes and the dwarf galaxies. After a detailed modelling of their properties, with particular attention to the coupling physics, we determine their 21 cm absorption line profiles. The infalling gas velocity around minihaloes/dwarf galaxies strongly affects the line shape and, with the low spin temperatures outside the virial radii of the systems, gives rise to horn-like line profiles. The optical depth of a dwarf galaxy is reduced for lines of sight penetrating through its H II region and, especially, a large H II region created by a dwarf galaxy with higher stellar mass and/or a top-heavy initial mass function results in an optical depth trough rather than an absorption line. We compute synthetic spectra of 21 cm forest for both high-redshift quasars and radio afterglows of gamma-ray bursts (GRBs). Even with the planned Square Kilometre Array (SKA), radio afterglows of most if not all GRBs would still be too dim to be the background sources for high-resolution (1 kHz) observations, but absorption lines can be easily detected towards a high-z quasar. Broadband observation against GRB afterglows can also be used to reveal the evolving 21 cm signal from both minihaloes and dwarf galaxies if there was no X-ray background or it was extremely weak, but it becomes difficult if an early X-ray background existed. Hence, the 21 cm absorption could be a powerful probe of the presence/intensity of the X-ray background and the thermal history of the early Universe.

Key words: line: profiles – galaxies: dwarf – galaxies: high-redshift – cosmology: theory.

1 INTRODUCTION

The formation of the earliest galaxies and the cosmic reionization is among the milestones in the history of the Universe. As the first stars form in the earliest non-linear structures, they illuminate the ambient intergalactic medium (IGM) and start the reionization process of hydrogen. Based on an instantaneous reionization model, the polarization data of cosmic microwave background (CMB) constrain the redshift of reionization to be $z_{\rm reion} \approx 10.5$ (Larson et al. 2010), while the Gunn–Peterson troughs (Gunn & Peterson 1965) shown in quasar (QSO) absorption spectra suggest that the reionization of hydrogen was very nearly complete by $z \approx 6$ (e.g. Fan, Carilli & Keating 2006). However, at present we are still unable to observe the earliest galaxies directly, and our current understanding on the reionization process is only based on theoretical models (e.g. Furlanetto, Zaldarriaga & Hernquist 2004) and simulations (e.g. Trac, Cen & Loeb 2008).

The most promising probe of the cosmic reionization is the redshifted 21 cm transition of H I which is directly related to the neutral component of the IGM (see e.g. Furlanetto, Oh & Briggs 2006 for a review). Unlike the Lyα resonance line, the 21 cm line could hardly be saturated because of its extremely small Einstein coefficient ($A_{10} = 2.85 \times 10^{-15}\,{\rm s}^{-1}$), so it traces well the reionization history, especially during the early stages. Using the CMB as the background radio source, 21 cm tomography could map out the three-dimensional structure of the emission or absorption of 21 cm photons by the IGM (e.g. Madau, Meiksin & Rees 1997; Tozzi et al. 2000). However, it requires the deviation of the spin temperature from the CMB temperature and may not be feasible for certain epochs; it could not resolve structures smaller than ∼1 Mpc; and it has a number of observational challenges (Furlanetto et al. 2006). Complementary to the 21 cm tomography, the 21 cm forest observation detects absorption lines of intervening structures against high-redshift radio sources (Carilli, Gnedin & Owen 2002; Furlanetto & Loeb 2002; Furlanetto 2006), and it is immune to most of the above difficulties encountered by the tomography observation. As it is very sensitive to gas temperature (Xu et al. 2009), it provides a useful tool to constrain the X-ray heating in the early Universe. Also, the 21 cm forest is a promising probe that could possibly detect high-redshift minihaloes, which are important for

★E-mail: xuyd@vega.bac.pku.edu.cn

determining the mean clumping factor of the IGM and putting limits on small-scale structure formation. Here, we focus on the absorption experiments and investigate the 21 cm absorption lines produced by the non-linear structures during the epoch of reionization.

The forest observation relies on the availability of luminous radio sources beyond the epoch of reionization. One possibility is the high-redshift quasars which have been observed up to $z = 6.43$ (Willott et al. 2007), and a radio-loud quasar at $z = 6.12$ was discovered by McGreer et al. (2006). Using high-z quasars or radio galaxies as backgrounds, Carilli et al. (2002) and Xu et al. (2009) have examined the possibility of detecting 21 cm absorption by the neutral IGM based on simulations. Another possible option is the radio afterglows of high-z gamma-ray bursts (GRBs). It is believed that some of the long-duration bursts are produced by the explosions of massive stars. The first stars are thought to be likely very massive, and may produce bright GRBs which would be detectable up to a redshift as high as 60 (Naoz & Bromberg 2007). Recently, GRB 090423 was discovered at $z = 8.1$ (Salvaterra et al. 2009, while Tanvir et al. 2009 reported its redshift to be $z = 8.26$), establishing the new redshift record of observation for all objects except for the CMB. The radio afterglow of a GRB can be observed out to a very late time when the outflow becomes sub-relativistic (e.g. Pihlström et al. 2007), and considering the cosmic time dilation, it offers us an adequate integration time. One possible problem with the GRB radio afterglow is that at very low frequency, synchrotron self-absorption may become important which may reduce the radio flux. None the less, some GRB radio afterglows may be sufficiently bright at the relevant frequency ranges.

In order to plan such observations, we need to know what kind of signals will be produced by the early structures, and to understand the physics behind the expected signals. In this paper, we provide a detailed modelling of the 21 cm absorption lines produced by minihaloes and dwarf galaxies during the epoch of reionization, and explore the physical origins of the line profiles. We generate synthetic spectra of both quasars and GRB afterglows, on top of which the 21 cm absorption lines are superposed. Projecting the capability of future instruments, we discuss the prospects of detecting the 21 cm signals from these non-linear objects in the early Universe.

This paper is arranged as follows. In Section 2, we describe the physical model involved with the 21 cm absorptions, including the halo model for high redshifts, the starburst criterion, a possible X-ray background, the physical processes taking place in minihaloes and dwarf galaxies, respectively, and the Lyα background produced by these early galaxies. In Section 3, we show the spin temperatures and 21 cm line profiles of minihaloes and dwarf galaxies for various parameters. Statistical results including line number density, theoretical spectrum and the equivalent width (EW) distribution are given in Section 4. Then, in Section 5 we study the feasibility of the 21 cm observation by making mock spectra of both quasar and radio afterglow of GRB. Finally, we summarize and discuss our results in Section 6.

Throughout this paper, we adopt the cosmological parameters from 5-year *Wilkinson Microwave Anisotropy Probe* (*WMAP*5) measurements combined with SN and BAO data: $\Omega_b = 0.0462$, $\Omega_c = 0.233$, $\Omega_\Lambda = 0.721$, $H_0 = 70.1\,\mathrm{km\,s^{-1}\,Mpc^{-1}}$, $\sigma_8 = 0.817$ and $n_s = 0.96$ (Komatsu et al. 2009).

2 THE MODEL

We start with a description of various aspects of physics involved with determining the absorption spectrum of 21 cm lines. This includes the high-redshift number density of dark matter haloes, gas distribution inside and around haloes, the criterion of star formation, the X-ray and Lyα background, and a detailed modelling of the physical properties of starless minihaloes and galaxies, respectively. Among these properties, the ionization state, the gas temperature distribution and the Lyα photon density are especially important for determining the strength and line profiles of the 21 cm absorption by minihaloes/dwarf galaxies.

2.1 The halo model

In order to model the halo number density at high redshift, we use the Sheth–Tormen halo mass function, which is based on an ellipsoidal model for perturbation collapse and fits well the simulation results. The comoving number density of haloes at redshift z with mass in the interval $(M, M + dM)$ can be written as (Sheth & Tormen 1999)

$$n(M, z)\,dM = F_{\rm ST}(\sigma, z)\,\frac{\bar{\rho}_0}{M}\,\frac{d\ln\sigma^{-1}}{dM}\,dM, \qquad (1)$$

where

$$F_{\rm ST}(\sigma, z) = A\sqrt{\frac{2a}{\pi}}\left[1 + \left(\frac{\sigma^2}{a\delta_{\rm sc}^2}\right)^p\right]\frac{\delta_{\rm sc}}{\sigma}\exp\left[-\frac{a\delta_{\rm sc}^2}{2\sigma^2}\right]. \qquad (2)$$

Here $\bar{\rho}_0$ is the cosmic mean density of the total matter today, $\sigma = \sigma(M)$ is the rms of a Gaussian density field smoothed on a mass scale M with a spherical top-hat filter of radius R, where R is equivalent to M in a fixed cosmology as $R = (3M/4\pi\bar{\rho}_0)^{1/3}$, and $\delta_{\rm sc} = 1.686/D(z)$ is the critical overdensity required for spherical collapse at redshift z, extrapolated to the present time using the linear theory, where $D(z)$ is the linear growth factor. The correction factors $a = 0.707$, $p = 0.3$ and $A = 0.3222$ were introduced as appropriate for ellipsoidal collapse (Sheth, Mo & Tormen 2001; Sheth & Tormen 2002).

The 21 cm signal depends on the gas content of minihaloes or galaxies, and the gas fraction in haloes will be suppressed by the heating processes during the reionization. Therefore, we set the lower limit of the halo mass to be the characteristic mass $M_{\rm C}$ at which haloes on average could only retain half of their baryons. The characteristic mass depends on the halo merger history and the thermal evolution of the Universe (Gnedin 2000; Okamoto, Gao & Theuns 2008). At high redshift that we are considering ($z > 6$), however, the filtering mass $M_{\rm F}$ provides a good fit to the characteristic mass $M_{\rm C}$ (Okamoto et al. 2008). Including the global heating process by an X-ray background (see Section 2.3), we compute the thermal evolution of the Universe and find that this mass scale is $\sim 10^6\,{\rm M}_\odot$ beyond redshift 7 for an early X-ray background not higher than 20 per cent of the intensity today. For high redshifts of interest, it is not very sensitive to the uncertain intensity of the X-ray background because of the delayed response of the gas density distribution to the change in the gas temperature. However, if the early X-ray background was as high as today, or even higher, it would have moderate effect in raising the Jeans mass and the filtering mass (see the right-hand panel of Fig. 2). So we take the halo mass range of $[10^6\,{\rm M}_\odot, 10^{10}\,{\rm M}_\odot]$ for an X-ray background not higher than 20 per cent of today's value, but also consider its effect on the minimum halo mass for higher intensities of the X-ray background (see Section 4). The range covers the characteristic halo mass and most of the galaxies that are responsible for the reionization (Choudhury & Ferrara 2007).

In the following, we use the NFW density profile for dark matter distribution inside of the virial radius $r_{\rm vir}$ of a halo (Navarro, Frenk & White 1997). In general, the key parameter in the NFW profile, the concentration parameter c, depends on the halo mass as well as its redshift. Unfortunately, the concentration parameter found from low-redshift simulations (Cooray & Sheth 2002) is not directly applicable to the epoch of reionization. Thanks to the resimulation technique, Gao et al. (2005) have simulated an example of the first haloes from very high redshift with extremely high resolution, and its density profile is derived in each resimulation at the final time. Here, we make use of their results. Assuming that c is inversely proportional to $(1 + z)$, as indicated by low-redshift results, we make a fourth-order polynomial fit to the simulated points in the logarithmic space of halo mass.

For the distribution of gas within the dark matter halo, we assume that the gas is in hydrostatic equilibrium with the dark matter, and have a spherical distribution. We expect gas in the high-z (and in general low-mass) galaxies has a rounder distribution rather than settling into a disc because (a) their circular velocities are comparable to the sound speed, making the gas more rounded than flat and (b) at such high redshifts, there may not be enough time for the gas to settle in a smooth disc. With the NFW profile of dark matter distribution, one can derive the gas density distribution analytically (Makino, Sasaki & Sudo 1998):

$$\ln \rho_{\rm g}(r) = \ln \rho_{\rm g0} - \frac{\mu m_{\rm p}}{2k_{\rm B}T_{\rm vir}} \left[v_{\rm e}^2(0) - v_{\rm e}^2(r) \right], \tag{3}$$

where $\rho_{\rm g0}$ is the central gas density, μ is the mean molecular weight of the gas depending on the ionization state, $m_{\rm p}$ is the proton mass, $k_{\rm B}$ is the Boltzmann constant and $T_{\rm vir}$ is the virial temperature of the halo. Here, $v_{\rm e}(r)$ denotes the gas escape velocity at radius r, which can be written as

$$v_{\rm e}^2(r) = 2\int_r^\infty \frac{GM(r')}{r'^2}\,{\rm d}r' = 2V_{\rm c}^2\, \frac{F(cx) + \dfrac{cx}{1+cx}}{xF(c)}, \tag{4}$$

where $V_{\rm c}^2 \equiv GM/r_{\rm vir}$ is the circular velocity at the virial radius, $x \equiv r/r_{\rm vir}$, c is the halo concentration and $F(c) = \ln(1 + c) - c/(1 + c)$. The maximum escape velocity is reached at the centre of the halo, $v_{\rm e}^2(0) = 2V_{\rm c}^2 c/F(c)$. In equation (3), the central density $\rho_{\rm g0}$ is determined by the condition that the total baryonic mass fraction within the virial radius is equal to $\Omega_{\rm b}/\Omega_{\rm m}$, which gives

$$\frac{\rho_{\rm g0}}{\bar\rho_{\rm m}} = \frac{(\Delta_{\rm c}/3)\,c^3\,(\Omega_{\rm b}/\Omega_{\rm m})\,e^A}{\int_0^c (1+t)^{A/t}\,t^2\,dt}, \tag{5}$$

where $\bar\rho_{\rm m} = \bar\rho_{\rm m}(z)$ is the mean matter density of the Universe at redshift z, $A \equiv 2c/F(c)$ and $\Delta_{\rm c}$ is the mean density of a virialized halo with respect to the cosmic mean value $\bar\rho_{\rm m}$ (Bryan & Norman 1998): $\Delta_{\rm c} = 18\pi^2 + 82(\Omega_{\rm m}^z - 1) - 39(\Omega_{\rm m}^z - 1)^2$, where $\Omega_{\rm m}^z = \Omega_{\rm m}(1+z)^3/[\Omega_{\rm m}(1+z)^3 + \Omega_\Lambda]$.

To determine the gas distribution outside $r_{\rm vir}$, one has to keep in mind that the gas slowly falls into the halo because of the gravitational force of the halo, so the gas has a peculiar (i.e. infalling) velocity which could be important for the 21 cm line. Also, due to the large cross-section at large radii, there is a high probability for the line of sight to go through these external parts of the haloes, and this infalling gas has to be included in the calculation. Barkana (2004) has derived a model for the expected profiles of infalling matter around virialized haloes based on the Extended Press–Schechter (EPS) formalism (Bond et al. 1991). This ‘Infall Model’[1] can also be used to compute the final peculiar velocity profiles around virialized haloes as well. The total velocity of the gas is the sum of the peculiar velocity and the Hubble expansion. In these infalling regions around haloes, we assume that the gas overdensity and velocity field follow the dark matter perfectly, with the scaling factor $\Omega_{\rm b}/\Omega_{\rm m}$.

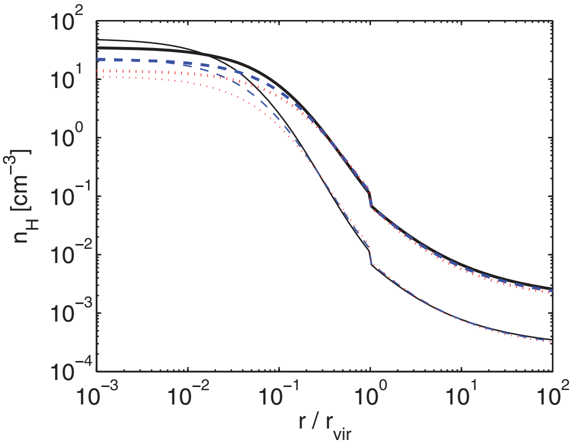

Figure 1. The hydrogen number density profiles in and around dark matter haloes of different masses: $M = 10^6\,{\rm M}_\odot$ (solid curves), $M = 10^7\,{\rm M}_\odot$ (dashed curves) and $M = 10^8\,{\rm M}_\odot$ (dotted curves), respectively. The thick curves are for redshift 20, while the thin curves are for redshift 10.

Several illustrative curves of the total hydrogen number density profiles are shown in Fig. 1 for various halo masses and two sets of redshifts. A constant hydrogen fraction of primordial value $X_{\rm H} = 0.752$ is assumed here (Spergel et al. 2007). The haloes with smaller mass and lower redshift are more concentrated. We can see that there are discontinuities at $r_{\rm vir}$. That is because when we adopt the gas density profile above, we are also assuming that the virialization shock is located right at the virial radius, and at the shock radius density and temperature jumps are expected. The exact position of the shock radius is subject to debate, and may depend on the assembly history of the halo. For a cosmology with $\Omega_{\rm m} = 1$, Bertschinger (1985) found that the accretion shock forms at the radius $R_{90.8}$ which encloses a mean dark matter density of 90.8 times the cosmic mean, while Abel, Bryan & Norman (2002) suggest that the shock radius is close to the virial radius. Below we assume that the shock is located at the virial radius, but note that the exact position of the shock radius has only a small effect on the resulting 21 cm signal (see the next section).

2.2 Star formation criterion

After the formation of dark matter haloes, some of the haloes could form stars inside while others could not, depending mainly on the cooling processes in each halo (see McKee & Tan 2008 for a recent review). As for those haloes with star formation, a starburst is more likely than continuous formation at this early epoch, because small objects are very sensitive to feedbacks and, therefore, as soon as the first stars formed in the galaxy, their radiation and induced supernovae could heat and eject the surrounding gas, quenching subsequent star formation. In order to determine whether a halo is able to undergo a starburst, here we use a time-scale criterion for star formation. If the time required for a halo to start forming stars is longer than the Hubble time at the halo redshift, it will remain starless, i.e. a system that is usually identified as a *minihalo*. Otherwise, the halo has enough time to cool and collapse to form stars, and becomes a *dwarf galaxy*. The time-scale required for turning on a starburst is modelled as the maximum between the free-fall time $t_{\rm ff}$ and the cooling time $t_{\rm cool}$, i.e. $t_{\rm SB} = \max\{t_{\rm ff}, t_{\rm cool}\}$, where

[1] Public code for this ‘Infall Model’ is available at http://wise-obs.tau.ac.il/~barkana/codes.html.

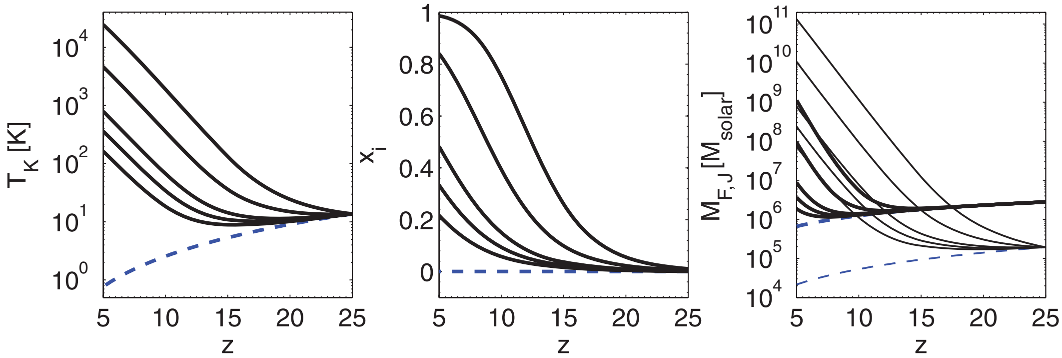

Figure 2. The evolution of the global temperature (left-hand panel), the mean ionized fraction (central panel) and the filtering mass and Jeans mass (right panel) of the IGM. The dashed curves are for $f_X = 0$, and the solid curves from bottom to top in each panel are for $f_X = 0.05, f_X = 0.1, f_X = 0.2, f_X = 1.0$ and $f_X = 5.0$, respectively. In the right-hand panel, the thin and thick curves illustrate the evolutions of the Jeans mass and the filtering mass, respectively.

$\sigma = 5.67 \times 10^{-5}\,\mathrm{erg\,cm^{-2}\,s^{-1}\,K^{-4}}$ is the Stefan–Boltzmann constant, and m_e is the electron mass. The evolutions of the IGM temperature and the mean ionized fraction caused by X-rays are shown in the left and central panels of Fig. 2 for several values of f_X. The case of $f_X = 0$ is denoted by the dashed curves. It corresponds to the situation in which there is no X-ray background, and the IGM temperature decreases adiabatically with a mean ionized fraction of 3×10^{-4} which is the residual electron fraction left over after the recombination. The solid curves from bottom to top in each panel take $f_X = 0.05, f_X = 0.1, f_X = 0.2, f_X = 1$ and $f_X = 5$, respectively. Here, we also illustrate the corresponding evolutions of the Jeans mass (thin curves) and the filtering mass (thick curves) in the right-hand panel of Fig. 2. The filtering mass, which provides a reasonable fit to the characteristic mass, is $M_F \sim 10^6\,\mathrm{M_\odot}$ for $f_X \lesssim 0.2$, $M_F \sim 2 \times 10^6\,\mathrm{M_\odot}$ for $f_X \sim 1$ and $M_F \sim 5 \times 10^6\,\mathrm{M_\odot}$ for $f_X \sim 5$ at $z \sim 10$.

The IGM creates a global decrement in the afterglow spectrum, on top of which minihaloes and dwarf galaxies produce deep and narrow absorption lines. The main broadening mechanism of each absorption line is the thermal broadening with the Doppler profile. The 21 cm optical depth of an isolated object is the integral of the absorption coefficient along the line of sight (Field 1959; Madau et al. 1997; Furlanetto & Loeb 2002):

$$\tau(\nu) = \frac{3h_P c^3 A_{10}}{32\pi^{3/2} k_B} \frac{1}{\nu^2} \times \int_{-\infty}^{+\infty} \frac{n_{\rm H\,I}(r)}{b(r) T_S(r)} \exp\left[-\frac{(u(\nu) - \bar{v}(r))^2}{b^2(r)}\right] \mathrm{d}x, \tag{14}$$

where $b(r)$ is the Doppler parameter of the gas, $b(r) = \sqrt{2 k_B T_K(r)/m_H}$, $u(\nu) \equiv c(\nu - \nu_{10})/\nu_{10}$ and $\bar{v}(r)$ is bulk velocity of gas projected to the line of sight at the radius r. Inside of the virial radius, the gas is thermalized, and $\bar{v}(r) = 0$, while the gas outside the virial radius has a bulk velocity contributed from both the infall and the Hubble flow according to the 'Infall Model'. The coordinate x is related to the radius r by $r^2 = (\alpha r_{\rm vir})^2 + x^2$, where α is the impact parameter of the penetrating line of sight in units of $r_{\rm vir}$.

The spin temperature of neutral hydrogen is defined by the relative occupation numbers of the two hyperfine structure levels, and it is determined by three competing processes: (1) absorption of CMB photons; (2) collisions with other hydrogen atoms, free electrons and other species; and (3) scattering with UV photons. The equilibrium spin temperature is given by (Field 1958; Furlanetto et al. 2006)

$$T_S^{-1} = \frac{T_\gamma^{-1} + x_c T_K^{-1} + x_\alpha T_C^{-1}}{1 + x_c + x_\alpha}, \tag{15}$$

where $T_\gamma = 2.726(1+z)$ K is the CMB temperature at redshift z, T_K is the gas kinetic temperature and T_C is the effective colour temperature of the UV radiation. In most cases, $T_C = T_K$ due to the frequent Lyα scattering (Furlanetto et al. 2006). The collisional coupling is described by the coefficient x_c, and x_α is the coupling coefficient of the Lyα pumping effect known as the Wouthuysen–Field coupling (Wouthuysen 1952; Field 1958). The main contributions to x_c are H–H collisions and H-$-e^-$ collisions, and it can be written as

$$x_c = x_c^{\rm eH} + x_c^{\rm HH} = \frac{n_e \kappa_{10}^{\rm eH}}{A_{10}} \frac{T_\star}{T_\gamma} + \frac{n_{\rm H\,I} \kappa_{10}^{\rm HH}}{A_{10}} \frac{T_\star}{T_\gamma}, \tag{16}$$

where $T_\star = 0.0682$ K is the equivalent temperature of the energy slitting of the 21 cm transition, and $\kappa_{10}^{\rm eH}$ and $\kappa_{10}^{\rm HH}$ are the de-excitation rate coefficients in collisions with free electrons and hydrogen atoms, respectively. These two coefficients at different temperatures are tabulated in Furlanetto et al. (2006). The coupling coefficient x_α is proportional to the total scattering rate between Lyα photons and hydrogen atoms,

$$x_\alpha = \frac{4P_\alpha}{27A_{10}} \frac{T_\star}{T_\gamma}, \tag{17}$$

where the scattering rate P_α is given by

$$P_\alpha = c\sigma_\alpha \frac{n_\alpha^{\rm tot}}{\Delta\nu_D} = 4\pi\sigma_\alpha J_\alpha. \tag{18}$$

Here $\sigma_\alpha \equiv \frac{\pi e^2}{m_e c} f_\alpha$ where $f_\alpha = 0.4162$ is the oscillator strength of the Lyα transition, $n_\alpha^{\rm tot}$ is the total number density of Lyα photons, J_α is the number intensity of the Lyα photons, and $\Delta\nu_D = (b/c)\,\nu_\alpha$ is the Doppler width with b being the Doppler parameter and ν_α being the Lyα frequency.

In addition to the global $\bar{x}_i(z)$ and $T_{\rm IGM}(z)$, to compute the line profiles of the 21 cm absorptions by minihaloes and dwarf galaxies, we need a detailed prescription of the ionization state, the temperature profile and the Lyα photon density in and around these objects. We model, respectively, these properties of both minihaloes and dwarf galaxies, as well as the intensity of Lyα background in the following.

2.3.1 Modelling the minihaloes

Minihaloes refer to those small haloes that are not capable of hosting stars, and they represent a very numerous population according to the halo mass function. As we are considering the early stages of reionization, when the IGM was slightly ionized with some rare sites illuminated by the earliest galaxies, the background radiation field has not been set up. However, the gas in minihaloes, which has much higher density, could be collisionally ionized partially, depending on its temperature. The H I fraction is computed from collisional ionization equilibrium (CIE)

$$n_{\rm e} n_{\rm H\,I} \gamma = \alpha_{\rm B} n_{\rm e} n_{\rm p}, \tag{19}$$

recombinations. On the other hand, x_c dominates over x_α for low-mass haloes which are almost completely neutral.

As for x_α, it has a very weak dependence on the redshift, but increases dramatically around $T_{\rm vir} \sim 10^4$ K due to the change of ionized fraction there. At higher temperatures, when the gas is almost collisionally ionized, the x_α slowly drops again because of the decreasing $\alpha_{\rm B}$ with temperature.

There are several effects taking place to determine the behaviour of x_c. In general, x_c increases with temperature because of the increasing collisional de-excitation rate $\kappa_{10}^{\rm HH}$ and $\kappa_{10}^{\rm eH}$. At low temperatures, x_c comes mainly from the H–H collisions, and the slowly decreasing x_c with increasing redshift is caused by the decreasing central density of hydrogen in less concentrated minihaloes at higher redshifts. The coupling changes from H–H collisions-dominated to e^-–H collisions-dominated as the temperature goes up, and this is in part responsible for the non-monotonic behaviour of x_c at $\log(T_{\rm vir}) \sim 4-4.5$. In addition, given a redshift, the concentration is lower for higher mass (higher $T_{\rm vir}$) haloes, and the central density of gas is lower. Therefore, $n_{\rm e}$ is smaller at high temperatures when the gas is almost ionized and $n_{\rm e}$ represents the total hydrogen density. This could also result in the non-monotonic behaviour of x_c.

2.3.2 Modelling the dwarf galaxies

As discussed in Section 2.2, starbursts could occur in some of the haloes, turning them into dwarf galaxies when the cooling process allows the gas to cool and collapse within a Hubble time. Depending on the initial mass function (IMF) and star formation efficiency, the stars produce a radiation field that will photonionize the gas creating an H II region, heat the gas around and produce Lyα photons at the same time. All these effects could have influences on the strength and shape of the 21 cm signal of the galaxy.

The IMF and the emission spectrum of the first galaxies remain very uncertain (see Ciardi & Ferrara 2005 for a review). However, Schaerer (2002, 2003) has examined spectral properties of the ionizing continua of high-redshift starburst galaxies for various IMFs, metallicities and star formation histories.[2] We make use of their results for the emitting rate of H and He$^+$ ionizing photons per solar mass of burst stars, denoted by $Q_{\rm H}$ and $Q_{\rm He^+}$, as well as the average energy per photon with $E > 54.4$ eV (He$^+$ ionizing threshold) denoted by $\bar{E}_{\rm He^+}$. The Lyman continuum photons are divided into two parts: photons with $E < 100$ eV could effectively result in photonionization, and those soft X-rays with $E > 100$ eV have a large probability to escape, and serve as an extra heating mechanism in addition to the X-ray background outside the H II region. Assuming a simple power law for the high-energy tail of the emission spectrum, we extrapolate $Q_{\rm He^+}$ and $\bar{E}_{\rm He^+}$ to get the production rate of soft X-rays $Q_{\rm X}$ and their average photon energy $\bar{E}_{\rm X}$. Thus the production rate of ionizing photons is $Q_{\rm ion} = Q_{\rm H} - Q_{\rm X}$.

As we are considering an early reionization epoch when the UV background has not been set up, all the ionizing photons creating an H II region come from the stellar sources inside of the dwarf galaxy, i.e. the $Q_{\rm ion}$. Considering the soft spectra of stellar sources, we assume a sharp boundary for each H II region, i.e. $x_i = 1$ for $r \le R_{\rm H\,II}$, $x_i = \bar{x}_i(z)$ for $r > R_{\rm H\,II}$ and $r > r_{\rm vir}$, and $x_i = x_i(\rm CIE)$ for $R_{\rm H\,II} < r \le r_{\rm vir}$ when $R_{\rm H\,II} < r_{\rm vir}$. Further, we assume all the stars to be located at the centre of the galaxy, and neglect the Hubble expansion during the growth of the H II region, as its growth time is much shorter than the Hubble time. Starting from the starburst time, t_*, the evolution equation of the radius of an H II region is

$$n_{\rm H\,I}(R) 4\pi R^2 \frac{dR}{dt} = \dot{N}_\gamma(t) - \int_0^{R(t)} \alpha_{\rm B} n_{\rm e} n_{\rm p} 4\pi r^2 {\rm d}r, \qquad (21)$$

where $\dot{N}_\gamma(t)$ is the ionizing rate, and the second term on the right-hand side accounts for recombinations in the H II region. Here $\alpha_{\rm B} = \alpha_{\rm B}(10^4\,{\rm K}) = 2.59$

[2] Data are available at http://cdsarc.u-strasbg.fr/cgi-bin/Cat?VI/109

of the H II radius at its maximum value. As one could expect, the size of an H II region is very sensitive to the IMF due to the strong dependence of Lyman continuum production on stellar mass. Here, we are considering isolated H II regions around dwarf galaxies, but in reality the galaxies will be somewhat clustered. So the ionized regions may extend further. However, the clustering of the first galaxies is beyond the scope of this work, and we reserve this to future works.

Once an H II region is created, the gas inside rapidly approaches the temperature around 2×10^4 K (Meiksin 2009). For the 21 cm absorption which requires neutral hydrogen, it is more important to compute the gas temperature outside the H II region. Here, we include the heating by local soft X-rays emitted by the dwarf galaxies. While the stars in the galaxy are also emitting Lyα photons, the heating effect due to the repeated Lyα scattering is negligible (Chen & Miralda-Escudé 2004). So the evolution of gas temperature can still be described by equation (12), but with an extra contribution to the $\epsilon_{\rm X,h}$ from the local X-rays. The energy deposition rate of local soft X-ray heating is

$$\epsilon_{\rm X,g} = \mathcal{R} n_{\rm H\,I} (\bar{E}_{\rm X} - E_{\rm th}) f_{\rm X,h}, \tag{24}$$

where $\mathcal{R}$ is the ionizing rate by the soft X-rays, $E_{\rm th} = 13.6$ eV is the ionization threshold of hydrogen and $f_{\rm X,h}$ is the fraction of the primary electron energy deposited into heat. The X-ray ionizing rate can be written as $\mathcal{R} = Q_{\rm X}(t)\, M_\star \sigma_{\rm I}(\nu)/(4\pi r^2)$, where $M_\star = f_\star\,(\Omega_{\rm b}/\Omega_{\rm m})\, M$, and $\sigma_{\rm I}(\nu)$ is the photonionization cross-section of hydrogen (Meiksin 2009):

$$\sigma_{\rm I}(\nu) = \sigma_0 \left[\beta \left(\frac{\nu}{\nu_{\rm th}}\right)^{-s} + (1-\beta)\left(\frac{\nu}{\nu_{\rm th}}\right)^{-s-1} \right], \tag{25}$$

where $\sigma_0 = 6.30 \times 10^{-18}$ cm^2, $\nu_{\rm th} = 3.290 \times 10^{15}$ Hz corresponding to the ionization threshold 13.6eV, $\beta = 1.34$ and $s = 2.99$. The average frequency of photons with $E \geq 0.1$ keV is used here. As for $f_{\rm X,h}$, we use a handy fit by Valdés & Ferrara (2008), which is a function of ionized fraction x_i.

With the initial condition of the IGM temperature at the starburst time, we solve for the gas temperature around an H II region, and plot the results for a dwarf galaxy with $M = 10^7\,{\rm M}_\odot$ at redshift 10 in Fig. 6. We take $f_{\rm X} = 0.1$ as the fiducial value for the X-ray background. The solid, dashed and dotted curves are for the three IMF models used in Fig. 5. For illustration, we have assumed that the starburst occurred at the same time as the halo formation, and the temperatures are all evaluated at $t_{\rm value} = t_{\rm H} - t_{\rm F}$, where the most probable value for $z_{\rm F}$ is used. For comparison, the temperature profile for a starless minihalo of the same mass and redshift is also shown as the dot–dashed line. Inside the H II region, the temperature is fixed at 2×10^4 K, and it drops down very sharply at the ionizing front due to the lower heating rate outside, as we could expect for stellar sources. The main heating mechanism outside $r_{\rm vir}$ is the X-ray background heating.

Apart from ionizing photons and soft X-rays, the dwarf galaxy is also producing Lyα photons which are essential for determining the spin temperature of hydrogen. However, those Lyα photons directly emitted by the galaxy could hardly contribute to the coupling in the gas outside the H II region due to the extremely long diffusion time, and they will be blocked near the ionization front. It is the Lyα photons cascaded from soft X-rays that penetrate into the nearby IGM and effectively couple the spin temperature to the kinetic temperature of the gas (Chen & Miralda-Escudé 2008). So, the contributing Lyα photons near an H II region come from recombination, the Lyα background, as well as the soft X-ray cascading. Valdés & Ferrara (2008) have examined the fraction $f_{\rm Ly\alpha}$ of the primary energy of electrons ionized by X-rays that converts into Lyα radiation. Using their result, the Lyα production rate from cascading around the H II region is

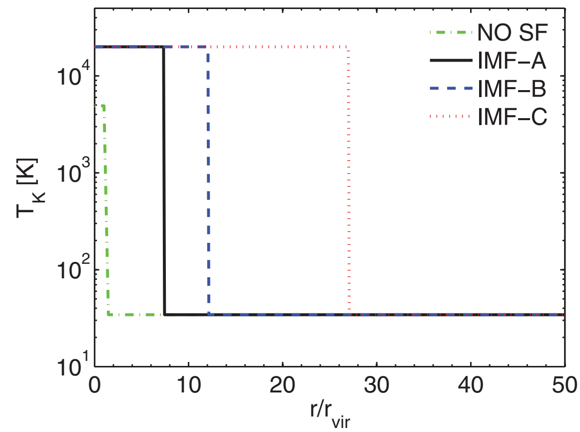

Figure 6. The temperature profiles of gas around a dwarf galaxy with mass $M = 10^7$ and metallicity $Z = 10^{-7}$ at redshift $z = 10$. The solid (black), dashed (blue) and dotted (red) curves are for Salpeter IMFs with mass ranges of 1–100 M$_\odot$ (IMF-A), 1–500 M$_\odot$ (IMF-B) and 50–500 M$_\odot$ (IMF-C), respectively. The temperature profile of gas if there is no star formation is also plotted with the dot–dashed (green) curve, and a fiducial value of $f_{\rm X} = 0.1$ is assumed for the X-ray background.

$$\dot{n}_{\rm Ly\alpha} = \mathcal{R} n_{\rm H\,I} \frac{\bar{E}_{\rm X} - E_{\rm th}}{h\nu_\alpha} f_{\rm Ly\alpha}, \tag{26}$$

where $\nu_\alpha = 2.47 \times 10^{15}$ Hz is the frequency of Lyα photons. The total number density of Lyα photons is obtained by integrating $\dot{n}_{\rm Ly\alpha}$ over an accumulating time $t_{\rm acc}$.

In this case, the accumulating time of Lyα photons is $t_{\rm acc} = \min\{t_{\rm diffu}, t_{\rm Xray}, (t_{\rm H} - t_{\rm s})\}$, where $t_{\rm diffu}$ is the Lyα diffusion time as before, but we take the mean-free path (MFP) of the soft X-rays as the $l_{\rm rms}$ here. $t_{\rm Xray}$ is the time during which the dwarf galaxy is producing X-rays, and $(t_{\rm H} - t_{\rm s})$ is the time interval between the halo redshift and the starburst redshift. Because of the large MFP of the X-rays (compared to the $r_{\rm vir}$), the Lyα diffusion time is also very large in this case, even larger than the Hubble time. As a result, the Lyα accumulating time is determined by $(t_{\rm H} - t_{\rm s})$ for the cases with IMF-A and IMF-B, while for the case with IMF-C, the Lyα accumulating time is limited by the lifetime of the stars.

2.3.3 The Lyα background

In addition to the Lyα photons produced by recombination and those cascaded Lyα photons near galaxies, there is also an Lyα background. The Lyα background originates from the continuum photons to the blue side of the Lyα line emitted by the early galaxies, and its intensity becomes important at very high redshift (Chen & Miralda-Escudé 2008). Only photons with $\nu < \nu_\beta$ can be redshifted to ν_α, and all photons of higher frequencies will be absorbed at the Lyβ or higher resonance Lyman series lines. Let $E(\nu)$ be the number of photons emitted over stars' lifetime per baryon in one of the haloes that collapse to form stars and per unit of frequency. According to the stellar spectra we adopted from Schaerer (2003), $E(\nu)$ is well approximated as flat near the Lyα frequency, then the intensity of the continuum Lyα background can be written as (Chen & Miralda-Escudé 2008)

$$J_\alpha = \tilde{J}_0 \bar{E}_\alpha \nu_\alpha [F(z) - F(z_\beta)]. \tag{27}$$

Here, $\tilde{J}_0$ is the fiducial Lyα intensity corresponding to a photon density of one photon per hydrogen atom per log frequency,

$$\tilde{J}_0 = \frac{c n_{\rm H}}{4\pi \nu_\alpha}, \tag{28}$$

where $n_{\rm H}$ is the number density of hydrogen. $\bar{E}_\alpha = \bar{E}(\nu_\alpha)$ is averaged over all the galaxies in the mass range of our consideration, and we estimate this value from the spectrum data provided by Schaerer (2003). In equation (27), $F(z)$ is the fraction of mass bound in star-forming haloes,

$$F(z) = \int_{M_{\rm min}}^{M_{\rm max}} \frac{M}{\bar{\rho}_0} n(M, z) p_\star(M, z)\, {\rm d}M, \tag{29}$$

where $n(M, z)$ is the halo mass function and $p_\star(M, z)$ is the probability of having star formation for a halo with mass M at redshift z. We derive $p_\star(M, z)$ according to the star formation criterion given in Section 2.2. At $z = 20$, $J_\alpha \approx 3 \times 10^{-11}\,{\rm cm^{-2}\,s^{-1}\,sr^{-1}\,Hz^{-1}}$, while at $z = 10$, it has increased to $J_\alpha \approx 2 \times 10^{-10}\,{\rm cm^{-2}\,s^{-1}\,sr^{-1}\,Hz^{-1}}$ which is already important for the Wouthuysen–Field coupling effect.

The problem of Lyα background propagating into minihaloes is complicated. The situation in minihaloes would be different from that in the IGM because of their higher column densities of neutral hydrogen (typically $N_{\rm H\,I} \sim 10^{21}\,{\rm cm^{-2}}$). The Ly$\alpha$ scattering cross-section in a region of high density consists of a Doppler core with a typical width of $\Delta\nu_{\rm D} = b/\lambda_\alpha$ centred on the Lyα frequency, and Lorentzian wings outside the core. Once a photon is redshifted or scattered into the 'core' frequencies, the cross-section is large and its mean-free path becomes very short and is spatially confined within a small region with very long diffusion time. Thus, the photons which eventually make up the Lyα background come from the blue side of the Lyα line, at the edge of the 'core' and 'wing'. In the case of minihalo, however, these photons would be blocked at the surface of the minihalo. The redshift across the minihalo is also too small for bluer wing photons which is not blocked at the edge of the minihalo to get redshifted into the core–wing boundary region when they arrive at the centre of the halo.

Another possibility is to consider photons with such frequency that their optical depth through the minihalo is about 1. Such a photon would scatter once inside the halo. One scattering per photon is of course negligible for the coupling effect in itself, but the frequency of the photon would be changed after the scattering. If the frequency increases, then the photon cross-section becomes even smaller and would escape right away, but if the photon loses energy during the collision and shifts to lower frequency, the cross-section would be increased. Could such a change bring the photon from the 'wing' to the 'core'? The frequency ν of such a wing photon is given by $N_{\rm H\,I}(r_{\rm vir})\sigma_\alpha(\nu) = 1$, where $N_{\rm H\,I}(r_{\rm vir})$ is the column density of the minihalo from $r_{\rm vir}$ to its centre, and $\sigma_\alpha(\nu)$ is the scattering cross-section on the Lyα damping wing. For typical thermal velocity of the H atom in the minihalo, we estimate that the change of photon frequency in one scattering ${\rm d}\nu < 2.2 \times 10^{11}$ Hz, comparable to the size of the core. On the other hand, the frequency distance to the line centre for such a photon is $(\nu - \nu_\alpha) \sim 10^{13}$ Hz, so ${\rm d}\nu \sim 1$ per cent $(\nu - \nu_\alpha)$. Therefore, during one or even a few favourable scatterings the photon could not enter the core and should escape away. We conclude that with the exception of the surface, the Lyα background could not affect the spin temperatures of the minihaloes.

3 THE 21 CM LINE PROFILES

With the detailed models of gas density, velocity profile, ionization state, temperature evolution and the intensity of both local and global Lyα photons for the minihaloes and the dwarf galaxies described above, we are now ready to compute their spin temperature profiles and 21 cm optical depths. In this section, we show our results of these detailed profiles for a variety of parameters. Although it will be very challenging to resolve them with radio instruments in the near future, these analyses help us explore the physical origins of the line profiles and understand the physics behind.

3.1 The coupling effects and spin temperature

In Fig. 7, we plot the spin temperature as a function of distance from the halo centre for a minihalo (left-hand panel) and a dwarf galaxy (right-hand panel) of the same mass $M = 10^7\,{\rm M_\odot}$ at redshift $z = 10$. We have taken $f_{\rm X} = 0.1$ as the fiducial value for the X-ray background. In order to show the coupling effects, the kinetic temperature of the gas and the CMB temperature are also plotted. As we see clearly from the left-hand panel, the spin temperature of the minihalo is coupled to the gas kinetic temperature ($T_{\rm vir}$ of the halo) at the centre. The halo with $M = 10^7\,{\rm M_\odot}$ and $z = 10$ has $T_{\rm vir} \sim 5000$ K, and the gas is almost neutral in CIE. As a

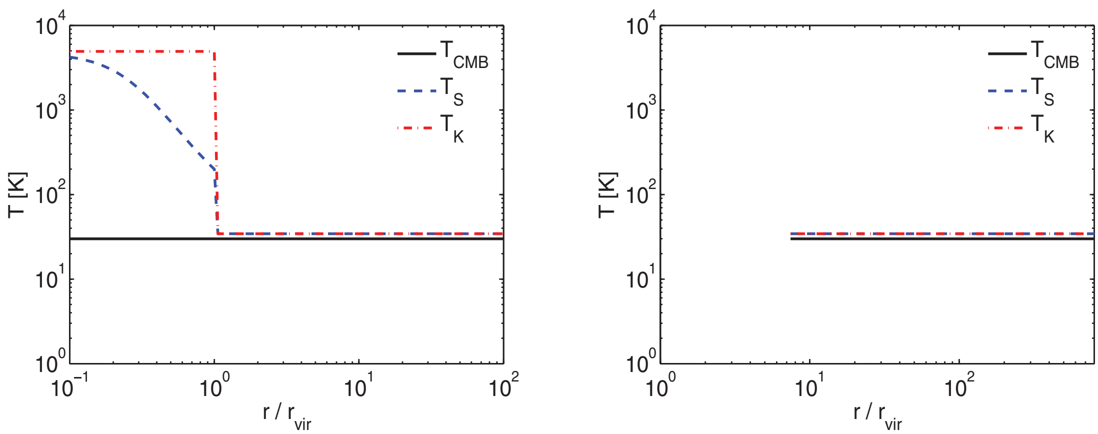

Figure 7. Spin temperature (dashed lines) and kinetic temperature (dot–dashed lines) profiles of a minihalo/dwarf galaxy with mass $M = 10^7\,{\rm M_\odot}$ at redshift 10. A fiducial value of $f_{\rm X} = 0.1$ is assumed for the X-ray background. The solid curves represent the CMB temperature. Left: the case for a minihalo in CIE. Right: the case for a dwarf galaxy which is photonionized after a starburst with IMF model-A and metallicity $Z = 10^{-7}$. The temperature curves are cut at the H II radius of 7.02 $r_{\rm vir}$.

result, the Lyα photons from recombination is totally negligible and the collisional coupling dominates. As the radius increases, the collisional coupling becomes less and less effective because of the decreasing density, and the spin temperature gradually decouples from the kinetic temperature. In addition to the dropping density, the collisional de-excitation rate coefficients ($\kappa_{10}^{\rm eH}$ and $\kappa_{10}^{\rm HH}$) also decrease due to the sharply decreasing kinetic temperature outside $r_{\rm vir}$, dramatically reducing the collisional coupling effect. However, the Lyα background at $z = 10$ is already strong enough to couple the spin temperature closely to the kinetic temperature of the gas. The recombination in the IGM also produces a significant amount of Lyα photons. As a result, $T_{\rm S}$ is always coupled to $T_{\rm K}$ outside minihaloes at $z = 10$.

As for the spin temperature profile of the dwarf galaxy in the right-hand panel of Fig. 7, the IMF model-A and a metallicity of $Z = 10^{-7}$ are assumed. We stop the $R_{\rm H\,II}$ and $T_{\rm K}$ evolution at $t_{\rm value} = t_{\rm H} - t_{\rm F}$, where $t_{\rm F}$ is the most probable formation time of this halo, and the spin temperature is also evaluated at this time. The left-hand side cut-offs of these curves are just the position of $R_{\rm H\,II}$ (7.02 $r_{\rm vir}$). As the H II radius of this galaxy is larger than the virial radius, the low density and low temperature outside the H II region make the collisional coupling very weak. In this case, the Lyα pumping is always the dominating coupling effect. The global Lyα photons from recombination and background flux dominate over the local Lyα photons from soft X-ray cascading, and just as the case outside a minihalo, the spin temperature sticks to the gas kinetic temperature.

Then, we investigate how the spin temperature changes with halo mass and redshift, and plot two sets of curves for various halo masses in Fig. 8, one (the thin set) for $z = 10$, and the other (the thick set) for $z = 20$. A fiducial value of $f_{\rm X} = 0.1$ is assumed here. For the minihaloes in the left-hand panel, the spin temperature is closely coupled to the kinetic temperature outside the $r_{\rm vir}$ for haloes at $z = 10$, in part because of the Lyα background, and in part because of the accumulated Lyα photons from recombination in the IGM that is partially ionized by the X-ray background. But at $z = 20$, both the Lyα background and the X-ray background are still weak, and $T_{\rm S}$ lies between the $T_{\rm CMB}$ and $T_{\rm K}$ for gas around minihaloes at this redshift. Inside the haloes, the density is larger at higher redshift, and the collisional coupling effect is correspondingly stronger, so the spin temperature is more tightly coupled to the virial temperature. On the other hand, haloes are more concentrated at lower redshift, and the slope of gas density profile is steeper. As a result the spin temperature drops more rapidly with radius at lower redshift. One different feature for the $10^8\,{\rm M}_\odot$ halo is that its spin temperature is effectively coupled to the gas kinetic temperature out to $r_{\rm vir}$, because for this relatively high-mass halo, its virial temperature ($\sim$1.5 × 10^4 K for $z = 10$, and $\sim$2.3 × 10^4 K for $z = 20$) is high enough to make the gas collisionally ionized ($x_i \sim 52$ per cent for $z = 10$, and $x_i \sim 98$ per cent for $z = 20$). With this partially ionized gas, Lyα photons from recombinations are effectively trapped, and serve as a strong coupling agent.

In the right-hand panel of Fig. 8, the spin temperature profiles for dwarf galaxies are all cut off at their H II radii at the left-hand side. For the case of $10^6\,{\rm M}_\odot$ dwarf galaxy, due to the much lower star formation efficiency ($f_\star \sim 4 \times 10^{-5}$, which increases to $\sim$0.03 for a galaxy with $10^8\,{\rm M}_\odot$) (Salvadori & Ferrara 2009), it could only create a very small H II region ($R_{\rm H\,II} \sim 0.008 r_{\rm vir}$ for $z = 10$ and $R_{\rm H\,II} \sim 0.02 r_{\rm vir}$ for $z = 20$). As for the galaxies with $10^7\,{\rm M}_\odot$ and $10^8\,{\rm M}_\odot$, they have larger stellar masses and create larger H II regions. So they have much less gas which could contribute to the 21 cm line absorption.

3.2 The absorption line profiles

Consider an isolated minihalo with mass $M = 10^7\,{\rm M}_\odot$ at redshift $z = 10$ for which we compute the optical depth as a function of frequency using equation (14). Results are shown in the left-hand panel of Fig. 9 for different impact parameters of the lines of sight. Very interesting features can be seen in the shown profiles. First, there are two peaks which sandwiched the centre of the line for impact parameters $\alpha = 1$ and $\alpha = 3$, showing horn-like profiles; secondly, as the impact parameter increases, the peak optical depth is *not* always decreasing. These two points are related issues, and they are both caused by the infalling gas with low spin temperature outside the minihalo.

To clearly see the origin of these interesting profiles, we have to understand the different contributions to the 21 cm absorption from the gas located at different radii. Because of the infall, the absorption line produced by the gas at the far side of the halo is blueshifted, while that produced by the gas at the near side of the halo is redshifted. Let $\nu_{\rm p}(r)$ be the peak frequency of optical depth created by gas located at radius r, and according to the integrand in

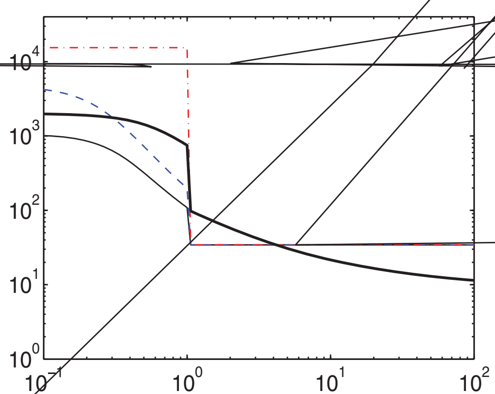

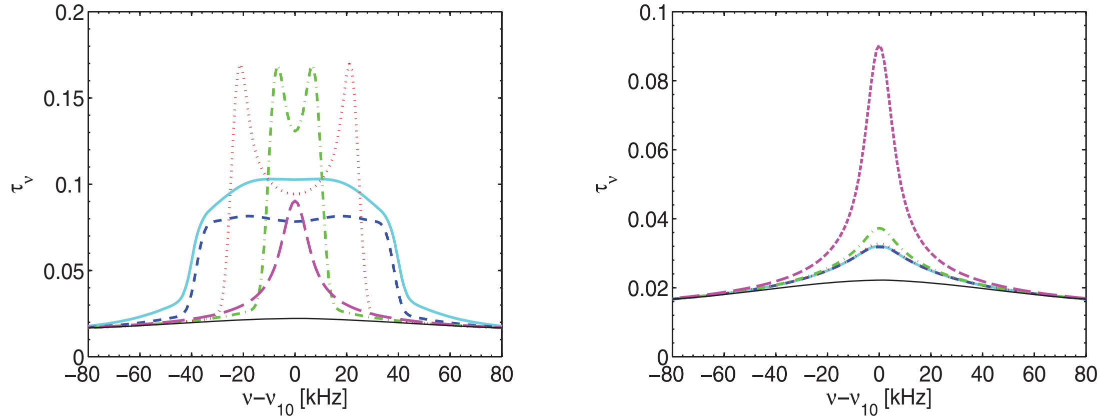

Figure 9. Optical depth profiles of a minihalo/dwarf galaxy with mass $M = 10^7\,\mathrm{M}_\odot$ at redshift 10. All the curves take $f_\mathrm{X} = 0.1$. The impact parameters of the thick curves are $\alpha = 0$ (solid cyan), 0.3 (short-dashed blue), 1 (dotted red), 3 (dot–dashed green) and 10 (long-dashed magenta), respectively, and the thin solid black curve is for $\alpha = 30$. Left: the case for a minihalo in CIE. Right: the case for a dwarf galaxy which is photonionized after a starburst with IMF model-A and metallicity $Z = 10^{-7}$.

equation (14), the absorption is shifted from the line centre by

$$\nu_\mathrm{p}(r) - \nu_{10} = \frac{\bar{v}(r)}{c}\nu_{10}. \tag{30}$$

Considering a line of sight passing through a minihalo with $M = 10^7\,\mathrm{M}_\odot$ and $z = 10$ from the centre ($\alpha = 0$), we divide the integration into segments, each of which has a contribution from a length of $1\,r_\mathrm{vir}$ on the line of sight. Then, we plot every absorption line created by one segment in Fig. 10. In the upper panel, the absorption line produced by the gas inside of r_vir is shown as the dashed curve, the solid lines from right to left correspond to the absorptions by segments of $(1-2)\,r_\mathrm{vir}$, $(2-3)\,r_\mathrm{vir}$, $(3-4)\,r_\mathrm{vir}$, $(4-5)\,r_\mathrm{vir}$, $(5-6)\,r_\mathrm{vir}$ and $(6-7)\,r_\mathrm{vir}$, respectively, and the dot–dashed line represents the absorption by the segment of $(7-8)\,r_\mathrm{vir}$. In the bottom panel, the 12 solid lines from left to right correspond to the absorptions by segments of $1r_\mathrm{vir}$ each starting from $8r_\mathrm{vir}$, and the last curve on the right represents the integral absorption from 20 to $100r_\mathrm{vir}$.

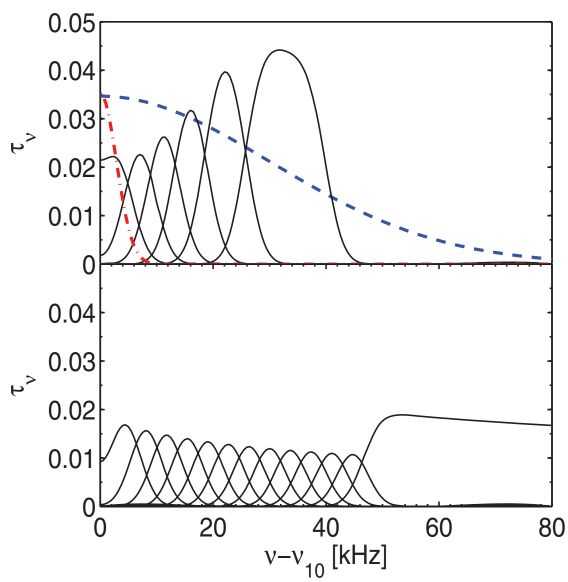

Figure 10. Different contributions to the optical depth from the gas at different radii. Upper panel: the absorption by gas inside of r_vir is shown as the dashed line; the solid lines from right to left correspond to the absorptions by segments of $(1-2)\,r_\mathrm{vir}$, $(2-3)\,r_\mathrm{vir}$, $(3-4)\,r_\mathrm{vir}$, $(4-5)\,r_\mathrm{vir}$, $(5-6)\,r_\mathrm{vir}$ and $(6-7)\,r_\mathrm{vir}$, respectively, and the dot–dashed line represents the absorption by the segment of $(7\text{–}8)r_\mathrm{vir}$. Bottom panel: the 12 solid lines from left to right correspond to the absorptions by segments of $1r_\mathrm{vir}$ each starting from $8r_\mathrm{vir}$, and the last curve represents the integral absorption from 20 to $100r_\mathrm{vir}$.

As can be seen clearly from Fig. 10, the virialized gas inside the minihalo has no bulk velocity, and the peak optical depth is located at the centre. The gas at $(1-2)\,r_\mathrm{vir}$ has the highest infall velocity, and the corresponding profile lies at the largest distance to the line centre in the upper panel. As the radius increases, the τ_ν profile gets closer to the line centre because of the lower infall velocity, and the optical depth decreases slowly with the decreasing density. One interesting feature is that there is a special position where the total velocity of the gas changes from negative (infall dominated) to positive (Hubble flow dominated), and at this turning point the two absorption lines created by the two segments on both sides of the minihalo converge into one at the line centre, and they contribute substantially to the central optical depth. For the minihalo with $M = 10^7\,\mathrm{M}_\odot$ and $z = 10$, this turning point lies at $7.3r_\mathrm{vir}$, and consequently the absorption by the segment of $(7-8)\,r_\mathrm{vir}$ peaks at the line centre. After that, the τ_ν profiles that come from larger radii leave the line centre again, because the infall velocity becomes even smaller and the total velocity (in the same direction as the Hubble flow) becomes more and more positive. Finally, when it goes out of the region influenced by the minihalo's gravity, and the density drops to the cosmic mean value, we recover the IGM optical depth.

The line profiles in Fig. 9 are better understood by noting that each is an integral of contributions from different radii. A substantial contribution to the optical depth comes from the outer region, because the gas outside r_vir has lower spin temperature. Especially, the gas in the infalling region on the far (near) side of the halo shares the same bulk velocity with the gas out of the region on the near (far) side, and they absorb the 21 cm photons at the same frequency. Therefore, the optical depth at the frequency range corresponding to the infalling region is increased a lot. In addition, the line profile gets narrower with lower temperature compared to the gas inside the halo, which further increases the peak value. As the impact parameter α increases from 0 to 1, more contribution comes from this cold region, so the peak optical depth increases. Also, the infall velocity shifts the peaks away from the centre, and results in the horn-like profile. As α increases further up to 3, the infall velocity decreases, and the two peaks move closer to each other. For α larger than the radius of the velocity turning point, the two peaks merge together and decrease slowly to the IGM optical depth as $\alpha \to \infty$.

The 21 cm profiles for an isolated dwarf galaxy for various impact parameters are shown in the right-hand panel of Fig. 9. Just as before, the spin temperature and the optical depth profiles are all evaluated at the time $t_{\rm value} = t_{\rm H} - t_{\rm F}$, and the most probable value for $z_{\rm F}$ is used. Thus we get an upper limit on the ionization, heating and Lyα coupling effects. The line profiles are completely different from the case of minihaloes. The horn-like profiles disappears and the absorption is strongly reduced for small impact parameters. The dwarf galaxy with $M = 10^7\,{\rm M_\odot}$ and $z = 10$ has an H II radius of $7.3r_{\rm vir}$, which is close to the turning point of the gas velocity. In other words, the hydrogen atoms inside $r_{\rm vir}$ and those within the infalling region are totally ionized, erasing the absorption features contributed by hydrogen in this region. Therefore, there will be only one peak at the centre no matter what the impact parameter is, and the optical depth is reduced for lines of sight which penetrate the H II region. As the impact parameter α increases, the optical depth first increases because more neutral gas near the H II region is intercepted by the line of sight. It reaches a maximum when $\alpha \approx R_{\rm H\,II}$ and then drops, approaching the IGM optical depth.

We also show the optical depth profiles for different halo masses and redshifts in Fig. 11. Here we also take $f_{\rm X} = 0.1$ for the X-ray background. In the left-hand panel, the case for minihaloes is shown. As we expected, the line profiles are broader for haloes with greater masses. That is because, on one hand, the virial temperature is higher for haloes of greater masses, which results in a broader Doppler profile for the absorption by gas inside the halo, and on the other hand, more massive haloes have stronger gravitational influence on the surrounding gas, and the induced higher infalling velocity shifts the absorption line farther from the line centre. In general, the absorption is stronger at higher redshift. The reason is that the IGM is denser at higher redshift and, also, the X-ray background is gradually set up as redshift decreases, and it heats and partially ionizes the gas in the IGM. As the frequency gets far from the line centre, the optical depths of all the minihaloes approach to the mean IGM value.

In the right-hand panel of Fig. 11, we show the 21 cm line profiles for dwarf galaxies with the same masses and redshifts as those for minihaloes in the left-hand panel. Starbursts with IMF model-A and metallicity $Z = 10^{-7}$ are assumed. An interesting feature emerges for the galaxy with $10^8\,{\rm M_\odot}$. Because of the higher star formation efficiency associated with higher mass galaxies, this dwarf galaxy creates a large H II region ($R_{\rm H\,II} \sim 38r_{\rm vir}$ for $z = 10$ and $R_{\rm H\,II} \sim 34r_{\rm vir}$ for $z = 20$) erasing all the absorption inside of it. As a result, a broad optical depth trough is produced instead of an absorption line! In the case of IMF model-C, the dwarf galaxy of the same mass could ionize an even larger H II region and hence could result in an even broader optical depth trough.

All the line profiles above are computed assuming that the minihalo or the dwarf galaxy is isolated. In real cosmic structures, a halo is surrounded by other haloes, and if we integrate the optical depth to a distance larger than the mean separation D of the haloes, we will probably hit another halo. So the integration should only be considered as reliable up to a distance of $D/2$. In practice, a $10^8\,{\rm M_\odot}$ halo, for example, might have many smaller haloes closer to it than another $10^8\,{\rm M_\odot}$ halo. Therefore, it is the mean separation of the smallest haloes we are considering, i.e. the haloes with $M = 10^6\,{\rm M_\odot}$ (for $f_{\rm X} \lesssim 0.2$), that determines the integration limit. We denote this mean separation as $D_{\rm min}$. The maximum impact parameter of a line of sight should also be $\alpha_{\rm max} = D_{\rm min}/2$. Integrating the optical depth up to $D_{\rm min}/2$, we plot optical depth profiles of a minihalo (blue dashed curve) and a dwarf galaxy (black solid curve) with $M = 10^7\,{\rm M_\odot}$ at $z = 10$ in Fig. 12. The line of sight is assumed to be passing through the minihalo/dwarf galaxy from the centre, and we set $f_{\rm X} = 0.1$. We see that the dwarf galaxy only produces a narrow and weak absorption line at the centre, because for this galaxy, only the gas in a sphere between the H II radius ($\sim 7.3r_{\rm vir}$) and $D_{\rm min}/2$ ($\sim 9.1r_{\rm vir}$) contributes to the absorption. In reality, however, the optical depth will not drop to zero at the boundaries of the absorption line but will connect with another line created by a neighbouring halo. In addition, as we mentioned before, the clustering of dwarf galaxies will extend their H II regions. Similarly, some minihaloes will be clustered around the dwarfs, and the surrounding gas in the infall region may be ionized, even if the minihaloes themselves can self-shield. Therefore, the clustering can reduce the 21 cm optical depth of some minihaloes and dwarf galaxies. Although the problem should ideally include the clustering properties of early galaxies, it is beyond the scope of this paper to include such features.

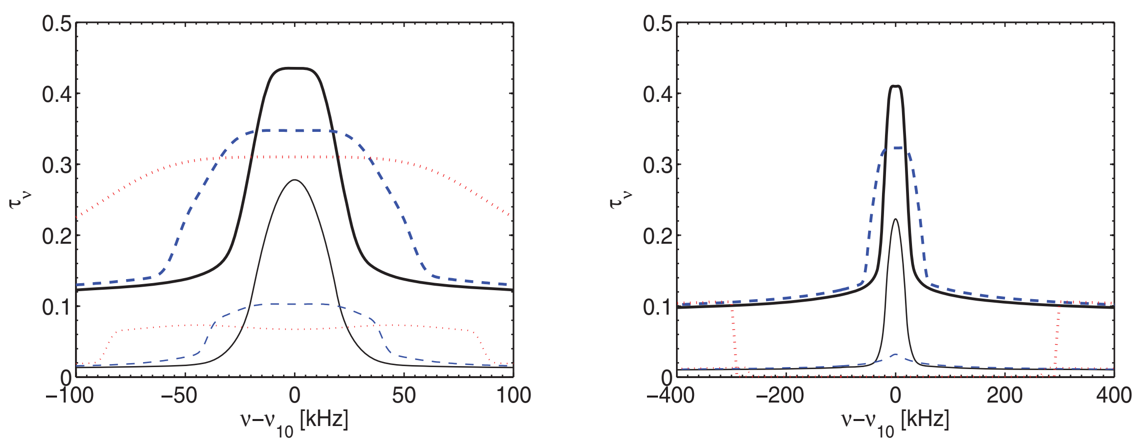

Figure 11. Optical depth profiles of minihaloes/dwarf galaxies with different masses: $M = 10^6\,{\rm M_\odot}$ (solid curves), $M = 10^7\,{\rm M_\odot}$ (dashed curves) and $M = 10^8\,{\rm M_\odot}$ (dotted curves), respectively. The thick curves are for redshift 20, while the thin curves are for redshift 10. All the curves take $f_{\rm X} = 0.1$. Left: the case for minihaloes in CIE. Right: the case for dwarf galaxies that are photoionized after a starburst with IMF model-A and metallicity $Z = 10^{-7}$. The impact parameter shown here is $\alpha = 0$.

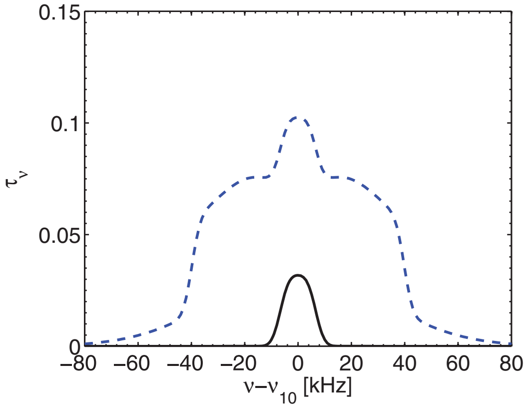

Figure 12. The optical depth profiles of a minihalo (blue dashed curve) and a dwarf galaxy (black solid curve) with $M = 10^7\ \mathrm{M_\odot}$ at $z = 10$. A starburst with IMF model-A and metallicity $Z = 10^{-7}$ is assumed for this galaxy. The optical depth at each point is integrated up to $D_{\min}/2$, the impact parameter is $\alpha = 0$ and the X-ray parameter is $f_X = 0.1$.

4 THEORETICAL SPECTRUM

In order to superimpose the 21 cm absorption lines of minihaloes and dwarf galaxies on to a radio spectrum of GRB afterglow, we first have to compute the line number density per unit redshift. Theoretically, including all (weak and strong) absorption lines, the number of halo intersections along a line of sight per redshift interval is

$$\frac{\mathrm{d}N}{\mathrm{d}z} = (1+z)^2 \frac{\mathrm{d}r}{\mathrm{d}z} \int_{M_{\min}}^{M_{\max}} n(M, z) A_{\max}\, \mathrm{d}M, \tag{31}$$

where $\mathrm{d}r/\mathrm{d}z$ is the comoving radial distance per redshift interval, $n(M, z)$ is the halo mass function given by equation (1) and $A_{\max} = \pi\alpha_{\max}^2$ is the cross-section (in physical coordinates) of a halo, in which the maximum impact parameter $\alpha_{\max}$ is set by half of the mean halo separation, i.e. $D_{\min}/2$, at each redshift. We plot the line number density as a function of redshift in Fig. 13 for three different values of $M_{\min}$, which are appropriate for different levels of the X-ray background. The curves are cut off at redshift $z = 8$ since our model applies only to the early stages of reionization, when the stellar sources have not set up an ionizing background.

This line number density is also the probability $P(z)$ that a line of sight intersects an object in a redshift interval dz centred on z.

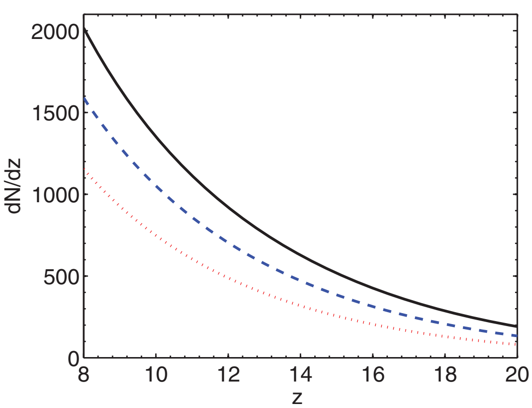

Figure 13. Theoretical evolution of line number density produced by minihaloes/dwarf galaxies along a line of sight. The maximum halo mass is $10^{10}\ \mathrm{M_\odot}$, and the minimum halo masses are $10^6\ \mathrm{M_\odot}$ (solid), $2 \times 10^6\ \mathrm{M_\odot}$ (dashed) and $5 \times 10^6\ \mathrm{M_\odot}$ (dotted), respectively.

In analogy), we
divide the o which
corresponds make
sure that the $\Delta z <$
0.01. Then, buted
in [0, 1)) fo if the
condition R

When an M for
the intersec halo
mass and th dshift
distribution oution
curve. Ther Sec-
tion 2.2 to dwarf
galaxy phot xy, its
metallicity given
by Salvador lways
$\gtrsim 10^{-4}$, the r ran-
domly sele each
object, we o and
dwarf galax 10) to
158 MHz (z $\mathrm{M_\odot}$,
out of whicl about
6.5 per cent e rest
come from τ) for
a range of hown
in Fig. 14. lts for
$f_X = 0, 0.05$ used
for $f_X \leq 0.$ e use
$M_{\min} = 5 \times$ es are
different be

As seen f w and
closely spac 21 cm
absorption ity of

the uncertain X-ray background. The absorption strength is significantly increased if there is no X-ray background, and it decreases rapidly with the increase of the X-ray background, which ionizes and heats the gas in the IGM reducing the optical depth of both non-linear structures and the global absorption. Especially, if the X-ray background in the early Universe was very strong (e.g. $f_X = 5$), which resulted from a large number of high-mass X-ray binaries in the case of top-heavy IMF towards high-z or from mini-quasars, we could hardly see any feature on a spectrum. This is because, on one hand, the line number density is reduced, and on the other hand, the absorption by non-linear structures is so weak that most lines are covered by the global absorption. For some minihaloes, the gas outside $r_{\rm vir}$ contributes to the absorption far from the line centre because of the infall velocity, and a few absorption lines of the neighbouring haloes overlap with each other on the wings. In this case the actual optical depth of each point is the sum over all the absorptions caused by these overlapping lines.

We compared two spectra: one taking into account the local X-rays contributing to heating and cascading to Lyα photons, and the second neglecting the above. It turns out that for the IMF model-A and the relatively high metallicities that are used in the spectrum, the small amount of soft X-rays produced by the dwarf galaxies make little difference (less than 0.1 per cent) even without an X-ray background. So we could not see any signature that can be attributed to them in the spectrum. However, if a dwarf galaxy with relatively high mass and (almost) primordial composition does exist, a top-heavy IMF (like the IMF model-C) is expected (Schneider et al. 2002, 2003), and the associated large H II region will result in a broad bump on the spectrum, erasing several absorption lines produced by neighbouring minihaloes.

Directly from the spectrum, we could compute the distribution of EW of the absorption lines for a specific range of observed frequency corresponding to a specific redshift. As the continuum of a background source has a global decrement due to the absorption of the diffuse IGM, the real signal of non-linear structures is the extra absorption with respect to the flux transmitted through the IGM. Therefore, the EW of an absorption line should be defined as

$$W_\nu = \int \frac{f_c e^{-\tau_{\rm IGM}(z)} - f_c e^{-\tau(\nu)}}{f_c e^{-\tau_{\rm IGM}(z)}}\, {\rm d}\nu = \int (1 - e^{\tau_{\rm IGM}(z) - \tau(\nu)})\, {\rm d}\nu, \qquad (32)$$

where f_c is the continuum flux of the background radio source, and $\tau_{\rm IGM}(z)$ is the optical depth of the diffuse IGM at redshift z. Using the theoretical spectrum of 129–133 MHz (corresponds to $z = 10.01$–9.68), we compute the cumulative distribution of EW of those 21 cm lines around $z \sim 10$, which is shown in Fig. 15. The dot–dashed, short dashed, solid, dotted and long dashed curves take $f_X = 0$, 0.05, 0.1, 0.2 and 1, respectively. As for the case of $f_X = 5$, the number of lines emerged from the IGM absorption in this frequency range is too small to derive any statistical implication, so the distribution of EW is not shown for this case. For the fiducial value $f_X = 0.1$, the majority of absorption lines has EWs around 0.03 to 0.3 kHz. We see that the number of large signals is very sensitive to the presence and intensity of the X-ray background. If there is no X-ray background ($f_X = 0$), then about 95 per cent of absorption lines have $W_\nu > 0.1$ kHz. For the value $f_X = 0.05$, there are about 75 per cent of lines with $W_\nu > 0.1$ kHz, while for $f_X = 0.1$ and 0.2, this fraction drops to 45 and 15 per cent, respectively. If $f_X = 1$ or even higher, there will be no absorption line that gets $W_\nu > 0.1$ kHz.

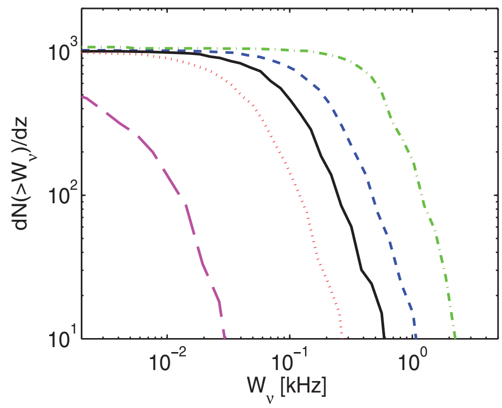

Figure 15. Cumulative distribution of EW of the 21 cm absorption lines around $z \sim 10$. The dot–dashed, short dashed, solid, dotted and long dashed curves are computed assuming $f_X = 0, f_X = 0.05, f_X = 0.1, f_X = 0.2$ and $f_X = 1.0$, respectively.

5 THE OBSERVABILITY

There are two kinds of radio sources which are potentially usable for absorption line studies at high redshifts during the epoch of reionization. One is the high-redshift quasars, which are quite luminous, but so far no quasar has been confirmed at $z > 6.5$. The other candidate is the radio afterglows of GRBs. Although they are fainter than quasars, they are more likely to exist at higher redshifts. Also, they have simpler power-law spectra at low frequencies due to synchrotron self-absorption, so it may be easier to extract absorption signals from bright GRB afterglows. Here, we examine the observability of 21 cm signals on both spectra of these background sources.

As for the upcoming and planned low-frequency interferometers, a spectral resolution of 1 kHz is achievable for LOFAR (Low Frequency Array)[3] and SKA.[4] From the theoretical spectrum computed above, we get about one absorption line in every 8.4 kHz at $z \sim 10$ on average when we use $M_{\rm min} = 10^6\,{\rm M}_\odot$ (line overlapping is accounted), and the line density (per observed frequency interval) is lower for lower redshifts or higher $M_{\rm min}$. On the other hand, the linewidth ranges mostly from ∼1 to ∼5 kHz for haloes of different masses. So the instruments can marginally resolve these 21 cm lines. While resolving the detailed line profile is probably out of reach, the line counting is feasible as long as sufficiently bright radio sources can be found at high redshift.

To produce mock spectra matching real observations, we degenerate the theoretical spectrum to a resolution of 1 kHz, add Gaussian noise on to each pixel with the signal-to-noise ratio S/N = 5, and convolve it with a continuum of GRB afterglow as well as a radio spectrum of quasar. Two synthetic spectra are illustrated in Fig. 16 with the left-hand panel for a GRB afterglow and the right-hand panel for a quasar. We take $f_X = 0.1$ for both cases. The flux density of GRB afterglow is scaled to 100 μJy at 200 MHz and $z = 6$, which is achievable for the afterglow of an energetic GRB produced by explosion of a massive metal-free star at high redshift, with isotropic energy of 10^{54} erg (Ioka & Mészáros 2005), and the spectral index is taken to be $2 (F_\nu \propto \nu^2)$, which is appropriate for the synchrotron self-absorption spectrum at the frequencies of interest (Frail 2003). The quasar flux density is scaled to 20 mJy at 120 MHz and $z = 10$,

[3] http://www.lofar.org/index.htm
[4] http://www.skatelescope.org/

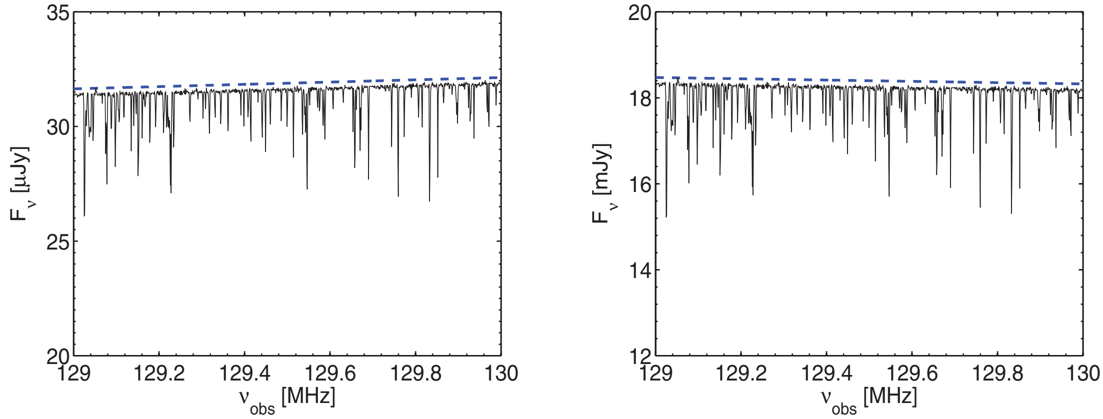

Figure 16. Synthetic spectra of 21 cm absorptions against a GRB afterglow (left-hand panel) and a quasar (right-hand panel) with 1 kHz resolution. The corresponding redshift is $z \sim 10$, and the unabsorbed continua are shown as the dashed (blue) lines. $f_X = 0.1$ is assumed for both spectra.

with a spectral index of -1.05 as fitted to the radio spectrum of the powerful radio galaxy Cygnus A (Carilli et al. 2002).

Apart from spectral resolution considerations, we also need high enough sensitivity to observe the absorption lines. In other words, with the planned instruments, the background source has to be bright enough to get the decrement of flux density higher than the detection limit. The minimum detectable flux density of an interferometer is related to the system temperature T_{sys}, the effective aperture area A_{eff}, channel width $\Delta\nu_{ch}$, integration time t_{int}, and S/N by

$$\Delta F_{min} = \frac{2k_B T_{sys}}{A_{eff}\sqrt{\Delta\nu_{ch} t_{int}}}\, \mathrm{S/N}. \tag{33}$$

The real signals of minihaloes or dwarf galaxies are their additional absorptions with respect to the absorption by the IGM, i.e. $\Delta F = F_\nu \exp(-\tau_{IGM}) - F_\nu \exp(-\tau)$. Equating this flux decrement to the detection limit, we get the minimum flux density of the background source required to observe the absorption lines:

$$F_{min} = 542\,\mu\mathrm{Jy} \left(\frac{\mathrm{S/N}}{5}\right) \left(\frac{0.1}{e^{-\tau_{IGM}} - e^{-\tau}}\right) \left(\frac{1\,\mathrm{kHz}}{\Delta\nu_{ch}}\right)^{1/2} \times \left(\frac{5000\,\mathrm{m^2\,K^{-1}}}{A_{eff}/T_{sys}}\right) \left(\frac{30\,\mathrm{d}}{t_{int}}\right)^{1/2}, \tag{34}$$

where the ratio A_{eff}/T_{sys} is an intrinsic parameter describing the sensitivity of an interferometry array, and we use the value for SKA here. For the GRB afterglow, the integration time is limited by its fading time-scale. Typically, after a bright, short-lived radio 'flare' at early times, the subsequent evolution of the radio afterglow can be described by a slow rise to maximum, followed by several segments of power-law decays with a time-scale of $\sim$100 d (Frail 2003). Here, we have assumed a reasonable integration time of 30 d, and find that a minimum flux density of $\sim$500 μJy is required to detect the absorption lines with the resolution of 1 kHz for the case of $f_X = 0.1$.

As seen from the continua (dashed lines) in Fig. 16, the flux density of our prototype GRB afterglow is more than one order of magnitude lower than this limit. Note that this is already an energetic GRB which is one order of magnitude brighter than normal GRBs. It may be possible that there are even brighter GRBs, but for most GRBs it seems that the radio afterglows would be too dim for being used as background source in observations with such a high spectral resolution. If we by chance find a quasar at very high redshift during the early stages of reionization, the signals could be easily detected. Especially, if one stacks together several lines to get an average profile, it will hopefully reveal the horn-like profiles we found.

Alter96nd3 p0.1 (l)-2.3 (f)-0.2s(It)-27-0.24han observal loRBs.-ound.

The existence of an X-ray background and its intensity is crucial in determining the observability of the signals. If there is no X-ray background, then with a GRB at redshift 9.8 and with the pixel resolution of $\Delta\nu_{\rm ch} = 1.38$ MHz, we can get 19 bands, and then 19 values of $D_{\rm A}$. We plot the $D_{\rm A}$ as a function of observed frequency in the upper panel of Fig. 17, and with the Gaussian noises of S/N = 5, the expected spectrum after the absorption by minihaloes and dwarf galaxies F_ν is shown in the bottom panel of Fig. 17. The original continuum $F_{\rm c}$ and the flux density absorbed by the homogeneous IGM $F_{\rm IGM}$ are also shown for comparison. With SKA, we could hopefully detect the non-zero $D_{\rm A}$s if $f_{\rm X} = 0$ or it is extremely small, which are signals from both minihaloes and dwarf galaxies. In addition, $D_{\rm A}$ decreases statistically with the decreasing redshift, which is a clear signature of the evolution of non-linear structures during the epoch of reionization. In the case of $f_{\rm X} = 0.05$, we could marginally observe 2 pixels on a spectrum from 131.5 to 158 MHz, one of which has a band width of ∼8 MHz (131.5–139.5 MHz) with the mean flux decrement of $D_{\rm A} \approx 0.017$, and the other has a band width of ∼18.5 MHz (139.5–158 MHz) with the mean flux decrement of $D_{\rm A} \approx 0.009$. However, if $f_{\rm X}$ takes our fiducial value 0.1, then even one band spanning the whole spectrum from the source to the lower redshift limit is still not broad enough to make the observation feasible. The situation gets worse for higher values of $f_{\rm X}$. Thus, the 21 cm broad-band observation against high-redshift GRBs can be a powerful probe of the presence and the intensity of the early X-ray background and the thermal evolution during the epoch of reionization.

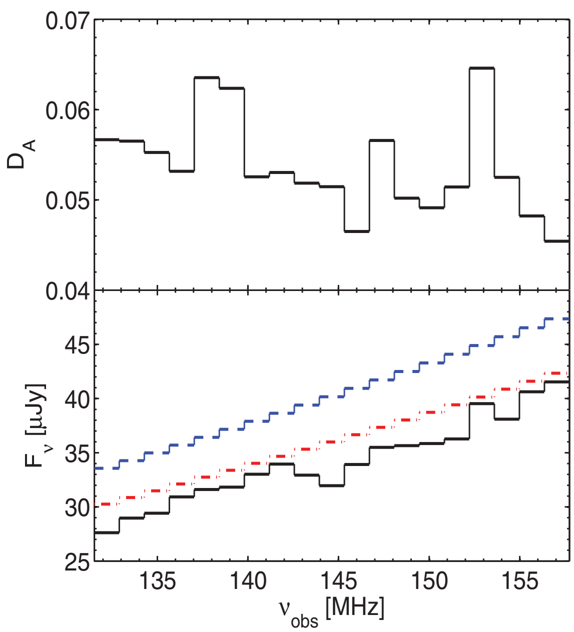

Figure 17. The mean flux decrement with respect to the continuum absorbed by the diffuse IGM (upper panel) and the synthetic broad-band spectrum with 1.38 MHz resolution (bottom panel) in the case of $f_{\rm X} = 0$. The 19 pixels show the frequency range corresponding to the redshift range from 9.8 to 8. In the bottom panel, the dashed, dot–dashed and solid lines are the original continuum flux density, the flux density absorbed by the homogeneous IGM and the expected flux density after the absorption by minihaloes and dwarf galaxies, respectively.

6 DISCUSSION

We have modelled in detail the gas density and velocity profiles, ionization state, temperature profiles and Lyα photon production for both minihaloes and dwarf galaxies during the early stages of reionization when the IGM was still patchy. We also take into account an early X-ray background, which could partially ionize and heat the IGM, and suppress the formation of low-mass minihaloes. Using the detailed model, we investigate the spin temperature of neutral hydrogen at different radii and the optical depth profiles of 21 cm absorption lines, for various impact parameters, halo masses and redshifts.

We find that the Lyα background and the Lyα photons from recombinations in the slightly ionized IGM couple the spin temperature to the kinetic temperature outside minihaloes or H II regions of dwarf galaxies, and the coupling is already strong at redshift 10. The Lyα background photons are blocked at surfaces of haloes, and the Lyα photons from recombinations are negligible inside low-mass haloes, though it dominates over the collisional coupling in high-mass haloes in which the gas is partially ionized by collisions. The collisions also couple the spin temperature to the gas kinetic temperature effectively at the centre, but this coupling and the spin temperature decrease with increasing radius.

The infall velocity of gas around the minihaloes/dwarf galaxies plays a very important role in determining the profiles of the 21 cm lines and double-peaked horn-like profiles are produced for a vast range of parameters. The line profile of a dwarf galaxy also depends on the size of its H II region, and hence its radiative properties. The horn-like profile disappears for galaxies which are large, or with top-heavy IMF so that the H II region expands beyond the turning point of gas velocity. The optical depth of a dwarf galaxy is lower for lines of sight penetrating through its H II region, while a sufficiently large H II region will lead to an optical depth trough rather than an absorption line.

With the line number density based on halo mass function and a physically motivated criterion for star formation, we generate synthetic spectra of 21 cm forest by Monte Carlo procedure, and calculate the cumulative distribution of EW of the absorption lines. Most of these lines have EWs around 0.03–0.3 kHz for an X-ray background intensity parameter of $f_{\rm X} = 0.1$, and the number of strong signals with large EWs decreases significantly with increasing $f_{\rm X}$. We then study the observability of these signals. For high-resolution (1 KHz) observations, the GRB radio afterglows are too dim to be used as the background, but absorption lines should be easily detected for a high-redshift quasar. It is exciting to know that the Pan-STARRS[5] (the Panoramic Survey Telescope And Rapid Response System) is being developed which will be able to detect quasars up to redshift ∼7 and aims to find ∼20–50 quasars at $z \sim 7$. For broad-band observations, it is also possible to detect the absorptions against GRB radio afterglows if there is no X-ray background. Setting a lower redshift cut-off at $z_{\rm lim} = 8$, we find that the optimal redshift for the GRB is $z_{\rm GRB} \sim 9.8$. With a sensitivity of SKA, an S/N of 5 and a reasonable integration time, we could get measurements of mean flux decrement $D_{\rm A}$ for 19 bands along the line of sight, each with a channel width of 1.38 MHz. In this way, we could detect not only the signals from both minihaloes and dwarf galaxies, but also their evolution during the epoch of reionization. However, the detectability of 21 cm signals is very sensitive to the presence of an early X-ray background. If an early X-ray

[5] http://pan-starrs.ifa.hawaii.edu/public/home.html

background existed but was not strong, taking $f_X = 0.05$, we could marginally observe 2 pixels along the line of sight towards a GRB which is located at the optimal redshift of 9.8. None the less, for the value of $f_X = 0.1$ or higher, the signal will be impossible to be detected. Therefore, the 21 cm absorption could be a powerful probe of the presence/intensity of the X-ray background and the thermal history in the early Universe. However, we note that it is difficult to find a radio source before the IGM has been significantly ionized or heated, especially for a very bright high-redshift quasar.

Furlanetto & Loeb (2002) studied the 21 cm forest signals of minihaloes and early galaxies. Here, we have re-investigated this problem with different and more detailed modelling of various properties of these non-linear objects, an early X-ray background, as well as the Lyα background during the epoch of reionization. We found stronger absorption signals from both minihaloes and dwarf galaxies for an early X-ray background not higher than the level today. Given the many different model parameters adopted, this is not unexpected. There are many differences in the details of modelling between the two papers, but the main difference seems to be the IGM temperature. Furlanetto & Loeb (2002) have assumed a heated IGM with a simple form of its evolution with redshift, which is already heated up to 1000 K at $z = 10$. This lies between our cases of $f_X = 1$ and $f_X = 5$. But in our fiducial model, the gas temperature in the IGM is about 35 K at the same redshift for $f_X = 0.1$. This is appropriate for the early stages of stellar reionization, when the percolation has not occurred yet. In Furlanetto & Loeb (2002), the gas structure in the infalling region around minihaloes/dwarf galaxies is modelled with a self-similar solution of secondary infall found by Bertschinger (1985), while we have used the gas infall model developed by Barkana (2004) which is based on the EPS model and spherical collapse. The Bertschinger's solution has a power-law density profile of $\rho \propto r^{-2.25}$, which is much steeper than the Barkana's prediction. Our density and peculiar velocity structure of the infalling gas, with the lower spin temperature outside the minihaloes/H II regions, produce a higher optical depth and a horn-like profile, which was not found in Furlanetto & Loeb (2002). For the dwarf galaxies, Furlanetto & Loeb (2002) considered protogalactic discs, whereas we assume here a spherical symmetry in the gas density distribution since the earliest galaxies are not likely to have large angular momentum.

In addition to the early X-ray background, an obvious uncertainty in our model is the production of soft X-rays by dwarf galaxies in the early Universe. Especially with the normal IMF model-A and relatively high metallicity, the amount of soft X-rays emitted after a starburst is very uncertain (Schaerer 2003). However, this amount of soft X-rays produced by stellar sources is always negligible as compared to the background X-rays even if $f_X = 0.05$. Another uncertainty comes from the gas density in minihaloes and dwarf galaxies. We have neglected the possible change of density profile after the star formation. The gas density profile could be modified by the expansion of the H II region when the ionizing front changes nature from R-type to D-type. There are also uncertainties in the star formation history in the dwarf galaxy. We have assumed that the feedback effects quench subsequent star formation (cf. Omukai & Nishi 1999), so that a single starburst is produced. We have also assumed a smooth gas density distribution, neglecting cool dense gas clumps from which the first stars are likely to form. Thus, we may have overestimated $R_{\rm H\,II}$, and the optical depth could be slightly higher if they are accounted for. On the other hand, the gas fraction in minihaloes or dwarf galaxies could be lower than the cosmic mean value (Naoz, Barkana & Mesinger 2009), then the optical depth will be lower. Also, the results depend on the assumption of $f_{\rm esc}$, which is taken to be 0.07, in agreement with current observations.

As illustrated in Figs 9 and 11, minihaloes and dwarf galaxies exhibit distinct optical depth profiles mainly due to the different ionization state and coupling physics, so they are potentially distinguishable. Although we may not be able to resolve the line profiles with the upcoming and planned instruments, it is encouraging to be able to distinguish their features in a statistical way, given that dwarf galaxies span a different halo population from minihaloes which cannot host stars. We reserve this investigation to future works.

ACKNOWLEDGMENTS

We deeply appreciate the insight of the referee and the constructive comments. We thank P. Dayal, S. Salvadori, W. Xu and B. Yue for helpful discussions; we are grateful to R. Barkana who provided his infall code. This work was supported in part by a scholarship from China Scholarship council, by a research training fellowship from SISSA astrophysics sector, by the NSFC grants 10373001, 10525314, 10533010 and 10773001, by the CAS grant KJCX3-SYW-N2 and by the 973 programme No. 2007CB8125401.

REFERENCES

Abel T., Bryan G. L., Norman M. L., 2002, Sci, 295, 93
Barkana R., 2004, MNRAS, 347, 59
Bertschinger E., 1985, ApJS, 58, 39
Bond J. R., Cole S., Efstathiou G., Kaiser N., 1991, ApJ, 379, 440
Bromm V., Larson R. B., 2004, ARA&A, 42, 79
Bromm V., Coppi P. S., Larson R. B., 2002, ApJ, 564, 23
Bryan G. L., Norman M., 1998, ApJ, 495, 80
Carilli C. L., Gnedin N. Y., Owen F., 2002, ApJ, 577, 22
Cen R., 1992, ApJS, 78, 341
Chen X., Miralda Escudé J., 2004, ApJ, 602, 1
Chen X., Miralda Escudé J., 2008, ApJ, 684, 18
Chiueh T., Lee J., 2001, ApJ, 555, 83
Choudhury T. R., Ferrara A., 2007, MNRAS, 380, L6
Ciardi B., Ferrara A., 2005, Space Sci. Rev., 116, 625
Cooray A., Sheth R., 2002, Phys. Rep., 372, 1
Fan X., Carilli C. L., Keating B., 2006, ARA&A, 44, 415
Field G. B., 1958, Proc. Inst. Radio Eng., 46, 240
Field G. B., 1959, ApJ, 129, 525
Frail D. A., 2003, preprint (astro-ph/0309557)
Furlanetto S. R., 2006, MNRAS, 371, 867
Furlanetto S. R., Loeb A., 2002, ApJ, 579, 1
Furlanetto S. R., Zaldarriaga M., Hernquist L., 2004, ApJ, 613, 1
Furlanetto S. R., Oh S. P., Briggs F. H., 2006, Phys. Rev., 433, 181
Gallerani S., Ferrara A., Fan X., Choudhury T. R., 2008, MNRAS, 386, 359
Gao L., White S. D. M., Jenkins A., Frenk C. S., Springel V., 2005, MNRAS, 363, 379
Gilfanov M., Grimm H.-J., Sunyaev R., 2004, MNRAS, 347, L57
Gnedin N. Y., 2000, ApJ, 542, 535
Gunn J. E., Peterson B. A., 1965, ApJ, 142, 1633
Hui L., Gnedin N. Y., 1997, MNRAS, 292, 27
Ioka K., Mészáros P., 2005, ApJ, 619, 684
Komatsu E. et al., 2009, ApJS, 180, 330
Lacey C., Cole S., 1993, MNRAS, 262, 627
Larson D. et al., 2010, preprint (arXiv:1001.4635)
Lin W. P., Jing Y. P., Lin L., 2003, MNRAS, 344, 1327
Madau P., Meiksin A., Rees M. J., 1997, ApJ, 475, 429
Makino N., Sasaki S., Sudo Y., 1998, ApJ, 497, 555
McGreer I. D., Becker R. H., Helfand D. J., White R. L., 2006, ApJ, 652, 157

McKee C. F., Tan J. C., 2008, ApJ, 681, 771
Meiksin A. A., 2009, Rev. Mod. Phys., 81, 1405
Naoz S., Bromberg O., 2007, MNRAS, 380, 757
Naoz S., Barkana R., Mesinger A., 2009, MNRAS, 399, 369
Navarro J. F., Frenk C. S., White S. D. M., 1997, ApJ, 490, 493
Oh S. P., Haiman Z., 2003, MNRAS, 346, 456
Okamoto T., Gao L., Theuns T., 2008, MNRAS, 390, 920
Omukai K., Nishi R., 1999, ApJ, 518, 64
Osterbrock D. E., 1989, Astrophysics of Gaseous Nebulae and Active Galactic Nuclei. University Science Books, Sausalito, CA
Pihlström Y. M., Taylor G. B., Granot J., Doeleman S., 2007, ApJ, 664, 411
Rauch M., 1998, ARA&A, 36, 267
Salvadori S., Ferrara A., 2009, MNRAS, 395, L6
Salvaterra R. et al., 2009, Nat, 461, 1258
Schaerer D., 2002, A&A, 382, 28
Schaerer D., 2003, A&A, 397, 527
Schneider R., Ferrara A., Natarajan P., Omukai K., 2002, ApJ, 571, 30
Schneider R., Ferrara A., Salvaterra R., Omukai K., Bromm V., 2003, Nat, 422, 869
Sheth R. K., Tormen G., 1999, MNRAS, 308, 119
Sheth R. K., Tormen G., 2002, MNRAS, 329, 61
Sheth R. K., Mo H. J., Tormen G., 2001, MNRAS, 323, 1
Spergel D. N. et al., 2007, ApJS, 170, 377
Tanvir N. R. et al., 2009, Nat, 461, 1254
Tegmark M., Silk J., Rees M. J., Blanchard A., Abel T., Palla F., 1997, ApJ, 474, 1
Tozzi P., Madau P., Meiksin A., Rees M. J., 2000, ApJ, 528, 597
Trac H., Cen R., Loeb A., 2008, ApJ, 689, L81
Valdés M., Ferrara A., 2008, MNRAS, 387, L8
Willott C. J. et al., 2007, AJ, 134, 2435
Wouthuysen S. A., 1952, AJ, 57, 31
Xu Y., Chen X., Fan Z., Trac H., Cen R., 2009, ApJ, 704, 1396

This paper has been typeset from a TEX/LATEX file prepared by the author.